Experiments in Fluids (2025) 66:32
https://doi.org/10.1007/s00348-024-03946-2

RESEARCH ARTICLE

Dynamic wall shear stress measurement using event-based 3d particle tracking

Christian E. Willert[1] · Joachim Klinner[1]

Received: 25 August 2024 / Revised: 14 December 2024 / Accepted: 16 December 2024

Abstract

We describe the implementation of a 3d Lagrangian particle tracking (LPT) system based on event-based vision (EBV) and demonstrate its application for the near-wall characterization of a turbulent boundary layer (TBL) in air. The viscous sublayer of the TBL is illuminated by a thin light sheet that grazes the surface of a thin glass window inserted into the wind tunnel wall. The data simultaneously captured by three synchronized event cameras are used to reconstruct the 3d particle tracks within 400 µm of the wall on a field of view of 12.0 mm × 7.5 mm. The velocity and position of particles within the viscous sublayer permit the estimation of the local vector of the unsteady wall shear stress (WSS) under the assumption of linearity between particle velocity and WSS. Thereby, time-evolving maps of the unsteady WSS and higher-order statistics are obtained that are in agreement with DNS data at matching Reynolds number. Near-wall particle acceleration provides the rate of change of the WSS which exhibits fully symmetric log-normal superstatistics. Two-point correlations of the randomly spaced WSS data are obtained by a bin-averaging approach and reveal information on the spacing of near-wall streaks. The employed compact EBV hardware coupled with suited LPT tracking algorithms provides data quality on par with currently used, considerably more expensive, high-speed framing cameras.

1 Introduction

Event-based vision (EBV), also termed *dynamic vision sensing* (DVS), is a new upcoming field within the field of computer vision and is inspired by the spiking mode of operation of the eye's retina. Contrary to conventional frame-based imaging, EBV only records changes of image intensity (i.e., contrast changes) on the pixel level, triggering a positive event (+1) for increasing intensity and a negative event (−1) for a decreasing intensity change. The typical threshold of the intensity change trigger is on the order of 10–20% but can be fine-tuned. As the pixels on the detector respond individually, the events appear asynchronously throughout the detector area resulting in a continuous stream of data, with each event datum $E_i = E_i(\mathbf{x}, t, p)$ consisting of pixel coordinates $\mathbf{x_i} = (x_i, y_i)$, a time stamp t_i, and a polarity $p_i \in \{+1, -1\}$ indicating the direction of the intensity change. Unlike to conventional imaging, intensity is not directly available and the random nature of the asynchronous stream of events necessitates completely different data processing algorithms that are subject of current research. For a recent review of the technology and underlying concepts, the reader is referred to the topical review by Gallego et al. (2022).

After original prototype and conceptual development of the technology in 1990s, affordable and ready-to-use hardware based on EBV only recently has become available with current sensor resolutions of 1 MPixel. This has broadened the range of applications as testified in a steadily increasing number of publications (see, e.g., Robotics and Perception Group 2023; Gehrig and Scaramuzza 2024).

The application of EBV for the visualization and measurement of fluid flows is by no means new. Initial work was performed by Drazen et al. (2011) on particle tracking velocimetry (PTV) of dense particles in a solid–liquid two-phase pipe flow using an EBV sensor of 256 × 256 pixels and continuous laser (5W) illumination. Ni et al. (2012) used an EBV array of 128×128 elements to demonstrate microparticle tracking (µPTV) with 12 µm microspheres and were able to detect Brownian motion. Using a stereoscopic EBV system, Wang et al. (2020b)

✉ Christian E. Willert
chris.willert@dlr.de

Joachim Klinner
joachim.klinner@dlr.de

[1] DLR Institute of Propulsion Technology, German Aerospace Center, 51170 Köln, Germany

Published online: 24 January 2025

implemented a 3d PTV system allowing them to reconstruct three-dimensional tracks combining 2d tracking results from two cameras. Their flow experiment consisted of a small hexagonal cell with a stirrer inducing a swirling flow containing O(100 µm) polystyrene spheres. First PTV measurements in an air flow were performed by Borer et al. (2017) using three synchronized EBV cameras (128× 128 pixels) to track helium-filled soap bubbles (HFSB) in volumes up to about 1 m side length using white light LED arrays for illumination. The flow was only sparsely seeded allowing individual particles to be tracked with final data sets containing up to O(1 000–10 000) tracks. More recently, Rusch and Rösgen (2023) re-implemented this concept as a real-time 3d PTV system enabling live flow field reconstruction.

The work presented herein extends upon the recently introduced event-based imaging velocimetry (EBIV) concepts (Willert 2023; Willert and Klinner 2022) and introduces a 3d-3c Lagrangian particle tracking (LPT) system in a macroscopic imaging configuration with a magnification of O(10 µm/pixel), thereby capable of resolving the flow at the viscous scale. In comparison with previous event-imaging implementations, much higher seeding densities are achieved. However, due to the high data load, the captured sequences of event data currently cannot be processed in real time and have to be analyzed in an offline fashion, that is, after completion of the measurement.

To demonstrate the viability of the proposed technique, the setup is used to acquire the near-wall trajectories of tracers within the viscous sublayer of a TBL, specifically to estimate the unsteady WSS. In this sense, the work addresses the current shortcoming of measurement techniques capable of providing reliable data of the unsteady WSS vector. The acquired data can be directly compared to readily available direct numerical simulations (DNS) at matching Reynolds numbers for this canonical TBL flow.

As pointed out in the review by Örlü and Vinuesa (2020), the measurement of the unsteady WSS remains a challenge with very few approaches capable of measuring the unsteady WSS directly, with the exception of a few micro-mechanical implementations such as the shear stress imaging device by Kimura et al. (1999) which relies on the measurement of the actual shear force acting on an array of transducers. The majority of WSS measurement devices rely on an indirect measurement, typically of the near-wall velocity in the region dominated by viscous forces, namely the viscous layer at the wall, which extends out to about 5 viscous units $l^* = \nu / u_\tau$. Here, ν is the kinematic viscosity of the fluid and u_τ the friction velocity which itself is related to the WSS τ_w and the fluid's density ρ by $u_\tau = \sqrt{\tau_w/\rho}$.

Aside from hotwire anenometry (HWA) and the micro-pillar method (Brücker et al. 2007; Große and Schröder 2008), most indirect WSS measurement techniques are particle-based methods, that is, variants of laser Doppler anemometry (LDA) or particle imaging. Among these, the following offer the desired combination of unsteady measurement of the WSS vector on a reasonable field of view (FOV), that is, they are not limited to point-wise measurements:

- Gnanamanickam et al. (2013), Liu et al. (2019) and Brücker (2015) used micro-pillars to get maps of the unsteady WSS. Some of the measurements were biased because the length of the pillars extended beyond the viscous layer.
- Using digital microscopic holography (µDH) (Sheng et al. 2008) or digital Fresnel reflection holography (DFRH) (Kumar et al. 2021), the TBL was imaged at a high magnification to retrieve unsteady 3d-3c flow data. Both techniques were applied in turbulent channel flow (TCF) in water.
- Near-wall particle image velocimetry (PIV) at high magnification generally provides data on the streamwise WSS component $\tau_{w,x}$ (de Silva et al. 2014; Willert et al. 2018; Wang et al. 2020a).
- Volumetric, near-wall PTV was used by Bross et al. (2019) to recover WSS information linking it to the three-dimensional dynamics of rare localized separation events within the viscous sublayer.
- Depth-from-defocus techniques, such as astigmatic µPTV (Fuchs et al. 2023) or multi-aperture micro-PTV (MAµ PTV) (Klinner and Willert 2024), image the particle field with the optical axis aligned to the wall-normal direction y.
- The "Shake the Box" (STB) technique (Schanz et al. 2016) provides time-resolved 3d-3c LPT data (Schröder et al. 2015, 2024) and, in terms of data provided, is most closely related to the approach presented herein.

The following article introduces a measurement configuration that can capture fields of the unsteady WSS vectors by tracking the motion of particles within the viscous sublayer using the novel event-imaging approach. The paper is organized as follows: the specifics of the event camera-based 3d-3c system are followed by a description of the data processing including the employed particle tracking algorithm and an error assessment. The results section concentrates on the variety of data that can be derived from the particle tracking data including near-wall flow statistics and derived WSS. The discussion positions the herein introduced event-based 3d PTV among existing approaches and addresses shortcomings of particle imaging-based WSS estimation.

2 3d-3c event-based tracking system

The 3d-3c particle tracking system comprises a triplet of event cameras (Prophesee EVK4, Sony IMX636 sensor, 1280×720 pixels, 4.86 µm pixel size) in a photogrammetric configuration, that is, arranged in a manner to capture a common, relatively thin volume of interest. Scheimpflug mounts on the two off-normal cameras allow a common plane of focus for all three cameras (Fig. 1a). The three cameras are synchronized with an external 1 MHz source to ensure a common time base. In addition, reference pulses at 100 Hz allow precise alignment of the separately recorded event sequences with a resolution of 1 µs with respect to one another (cf. Figure 2). This is necessary since the cameras operate in a continuous mode and cannot be started from a common well-defined trigger and consequently require a posteriori re-alignment of the streamed data.

In the present application, the tracking system is mounted below the wind tunnel section and observes the bottom layer of the TBL through a 1-mm thin glass window with anti-reflective coating. This domain is illuminated with a ≈ 0.5 -mm thin light sheet introduced from the side of the wind tunnel with a slight inclination ($\approx 0.5°$, cf. Figure 1b). The light sheet is oriented such that all cameras receive the light scattered by the tracers at a common scattering angle of 90°. This results in similar illumination intensities on all three detectors and avoids angle-dependent Mie scattering differences between the cameras.

At a working distance of about 200 mm, a common FOV of about $12.0 \times 7.5\,\mathrm{mm}^2$ is captured (magnification $m = 0.48$ with 10 µm/pixel). The pulsed laser (Innolas/Iradion, Nanio-Air 532-10-V-SP) is operated at a pulsing frequency of 5 kHz with an integral power of about 1–2 W and is synchronized to the camera time base (see Fig. 2). The macro-objective lenses (Nikon Micro-Nikkor 55 mm / 2.8) are stepped down to $f_{\#} = 8$.

Water-based tracer particles of about 1–2µm and a lifetime of about 10 min are provided by a fog generator (HazeBase Classic, base*M fluid). As detailed in Appendix 1, the temporal response of these tracers is estimated to be in the range of $3\,\mu\mathrm{s} < t_p < 12\,\mu\mathrm{s}$ with Stokes numbers well below unity, guaranteeing good flow following properties.

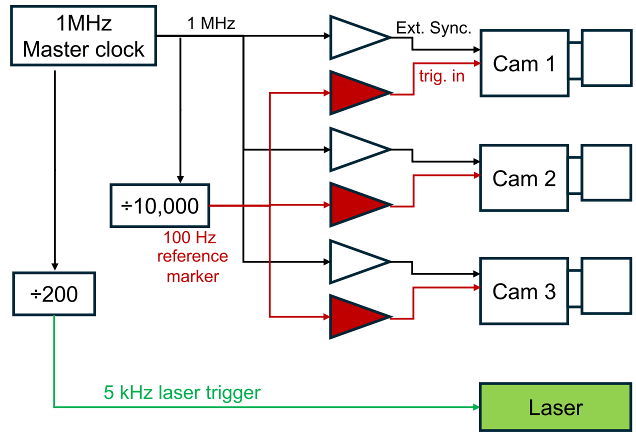

Fig. 2 Synchronization unit provides a common time base for all event cameras as well as a laser trigger

For the measurements, event recordings of up to 60 s duration are acquired at wind tunnel speeds of $U_\infty = 5.2$, 7.5 and $10\,\mathrm{m/s}$. Table 1 summarizes specific aspects of the acquired raw data such as event data rate and the amount of actual data streamed to the host computer. Table 1 also provides the TBL's characteristic parameters which were obtained by high-speed profile PIV (Klinner and Willert 2024).

Keeping the laser energy and light sheet position constant, the seeding density is varied by more than one order of magnitude resulting in a corresponding variation in the event data rates. The EBV camera settings—so-called *biases*—are adjusted for minimal pixel refractory time ("dead time" after event detection) and to favor positive (+1 events) as these were found to be more responsive than the bright-to-dark contrast changes (−1 events). The imbalance between positive and negative contrast change detection is a detector-specific behavior, a further investigation thereof being beyond the scope of this article. Figure 3 intends to

Fig. 1 Triple event camera setup placed below the 1-m wind tunnel of DLR in Göttingen for particle tracking in the viscous sublayer of a TBL (**a**), laser light sheet grazing the window at the observation area at an estimated angle of $\approx 0.5°$ to the surface (**b**)

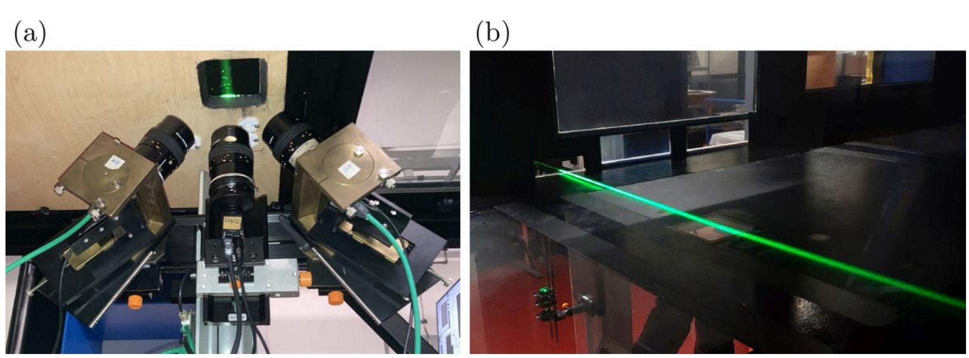

Table 1 Overview of acquired event data including characteristics of the studied TBL as determined with HS profile PIV

U_∞	[m/s]	**5.2**				**7.5**			**10.0**
Re_τ		563				754			935
u_τ	[m/s]	0.223				0.304			0.390
$l^* = \nu / u_\tau$	[µm]	68.8				50.5			39.4
δ_{99}	[mm]	38.7				38.1			36.8
Data set		5-3	5-1	5-4	5-2	7-1	7-3	7-2	10-1
Duration	[s]	60	60	60	60	10	10	10	10
Event rate	[10^6 Ev/s]	1.5	8.2	14.1	23.2	8.1	16.6	16.9	13.4
Pos. Events		97 %	85 %	77 %	75 %	89 %	80 %	80 %	81 %
Data rate[a]	[MB/s]	21	92	148	216	92	167	169	141
Track yield[b]		60 %	54 %	39 %	4.8 %	40 %	30 %	24 %	41 %

[a]combined for all three event cameras,

[b]tracks of length $N_{\text{track}} \geq 7$ after validation at a wall distance $[0.5 < y^+ 1.5]$

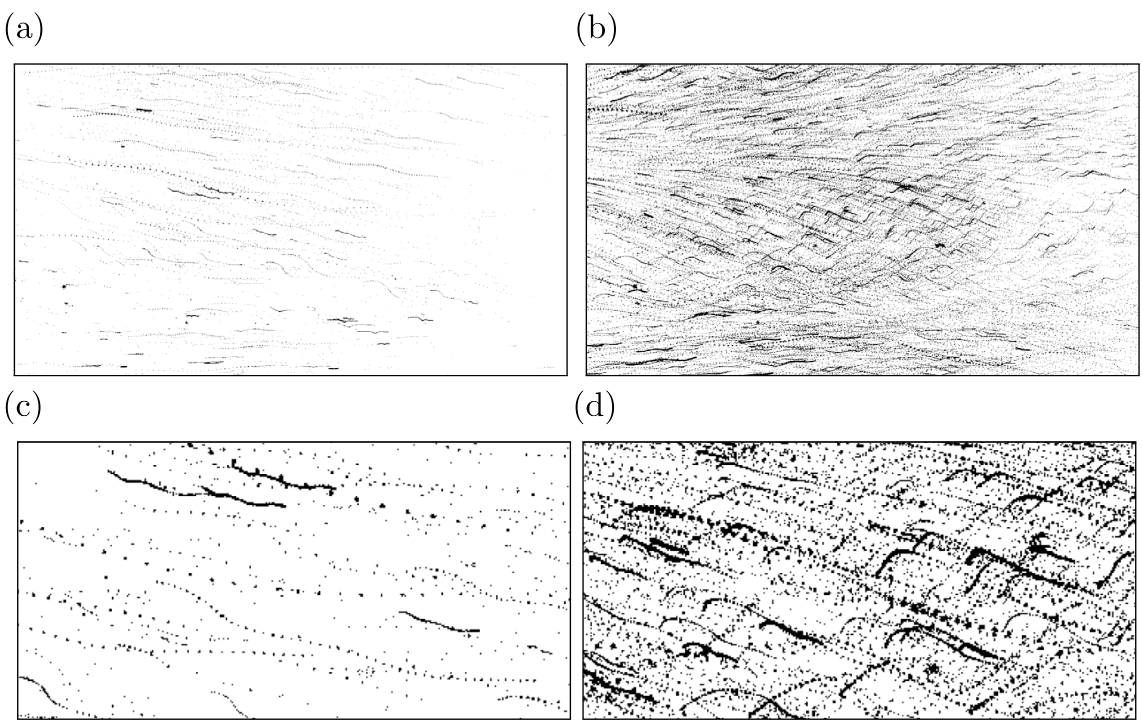

Fig. 3 Sample pseudo-images from 10 ms of the event stream recorded by the central camera at 1.5 Mev/s (**a**) and 23 Mev/s (**b**). The lower rows (**c**) and (**d**) show zoomed portions of the above. With a laser pulse rate of 5 kHz, the pseudo-images contain 50 laser pulses. Only positive (dark-to-bright) contrast changes are shown

provide an impression of the event data acquired by one of the cameras at two different seeding concentrations.

3 Camera calibration

Elemental for reliable 3d-PTV is an accurate camera mapping which allows a transformation from image space into object space and back. This is generally achieved using established camera calibration procedures.

Calibration data in the form of image–object correspondence points is collected from recordings of a calibration target. Here, a checker-board target with 1 mm × 1 mm squares printed on glass is mounted parallel to the observation window and traversed in wall-normal (y) direction at increments of $\Delta y = 250\,\mu\text{m}$ (Fig. 4a). Due to insensitivity of the EBV to static imagery, the glass target is back-illuminated by a pulsed LED at 100 Hz. Summing events over a period of 0.5 s provides high-contrast calibration images suitable for grid marker

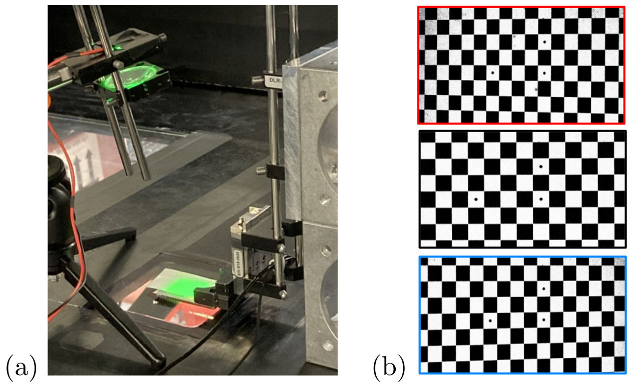

Fig. 4 Camera calibration setup using a back-illuminated checkerboard target mounted on a micro-translation stage (**a**), simultaneous camera views of the target (**b**)

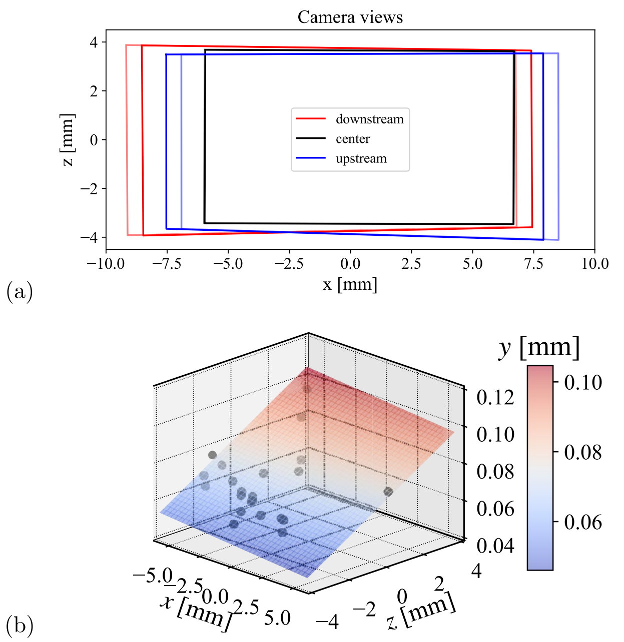

Fig. 5 Camera field of view at $y = 0$ and $y = 500\,\mu$m (**a**). Reconstructed plane of the glass insert based on 3d reconstruction of stationary particles stuck to the surface (**b**)

detection (Fig. 4b). The common FOV shared by the cameras, as depicted in Fig. 5, extends about 12 mm by 7.5 mm in streamwise and spanwise direction, respectively.

The accuracy of particle reconstruction in relation to the glass surface requires the knowledge of the plane spanned by the target in relation to the plane of glass surface. This is achieved by triangulation of stationary particles and dust attached to the surface of the window, which are readily detected in the raw event data as continuous triggered pixel clusters. A 2d plane fit provides the reference plane to which the reconstructed track data will be aligned (Fig. 5b). The slope amounts to about 50 μm across the 10 mm FOV (inclination ≈ 0.3 °).

A dual plane method is used to map between object and image space and to compute epipolar lines to match the particle images between the views. A particle-based residual alignment such as typically performed in 3d STB LPT is currently not applied.

4 Event data processing

Prior to particle tracking, the acquired event recordings are temporally aligned using the external 100-Hz reference markers and then converted to pseudo-image sequences by re-sampling the event data at a frequency corresponding to the laser pulsing rate. During a sample interval, e.g., 200 μs at 5 kHz laser pulsing, any given pixel is only allowed to produce at most one event. Hence, the resulting pseudo-image is binary in nature. The automated event sampling is performed on the basis of searching for the minimum in the ensemble averaged event histogram, a representative example of which is given in Fig. 6 for a laser pulsing frequency of 5 kHz. In this case, the sampling period, as indicated by the red dashed lines, would begin with an offset of ≈ 175 μs and end 200 μs later. As described in more detail in Willert (2023), the use of pulsed light intends to mitigate issues related to the delayed response, e.g., latency, of the event detector. This latency is apparent in Fig. 6b with events being registered by the detector up to

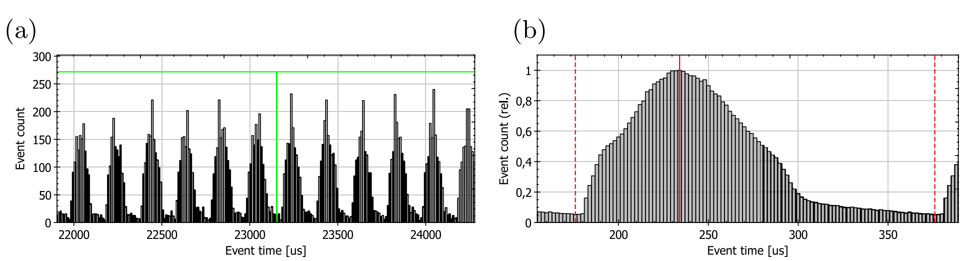

Fig. 6 Histograms of positive (+1) contrast change event data recorded by one of the three cameras with the laser pulsing at 5 kHz; green line indicates a periodic reference marker at 100 Hz used for registration of event streams to one another; (**a**) raw stream binned at 10 μs intervals, (**b**) mean event distribution during one pulsing period (200 μs)

100 µs after being exposed to the short pulse of light (about 20 ns). Another advantage of the pulsed light approach is the capture of stationary particles which would be “invisible" when illuminated by a continuous light source. Finally, the use of continuous illumination was found to “favor" slower particles since they have a higher likelihood of triggering events while crossing a given pixel. This would bias the measurement toward lower velocities already at the raw data stage (Willert 2023).

Particle tracking is performed for each camera view individually by first extracting contiguous binary pixel blobs from the pseudo-images and computing their centroids (center of mass). A k-d tree-based nearest neighbor search scheme then detects tracklets across three adjacent pseudo-images and extends these via a predictor scheme to the following image frames. The tracker accepts gaps of up to one pseudo-frame to prevent a premature truncation of tracks. Given the high variability of particle velocity and paths within a very thin volume, a multiple pass scheme is implemented: first, slow moving particles are tracked and removed from the pool of particle positions. By gradually increasing the initial search radius, the next tracking passes draw candidates from a gradually reduced pool of particle positions. This process is repeated 3 to 4 times.

Using the 2d tracks for the three cameras views, reconstruction of the 3d tracks is performed using the epipolar lines of a given particle on the other two views. Using a cubic B-spline fit on the raw 3d position data yields a set of spline coefficients and provides a continuous description of the particle’s position, velocity, and acceleration along the track, that is, in time and space. The spline fit is weighted proportionally to the inverse of the residuals of the 3d particle position. Track validation is based on the residuals of the cubic spline fit ($r_{\mathrm{fit}} \leq 10\,\mu\mathrm{m}$), a minimal track length ($N_{\mathrm{track}} \geq 7$), and maximum allowed wall-normal fluctuation ($v_{\mathrm{rms}} < 0.02 U_\infty$ for $y^+ < 2$).

The wall shear stress vector $\vec{\tau}_w = [\tau_{w,x}, \tau_{w,z}]$ for each validated particle position is then obtained be dividing its estimated wall parallel velocity $\mathbf{u} = [u, 0, w]$ by its distance from the wall Δy as an approximation to the definition of WSS

$$\vec{\tau}_w = \mu \left.\frac{\partial \mathbf{u}}{\partial y}\right|_{y=0} = \mu \lim_{y \to 0} \frac{\mathbf{u}(y)}{y} \approx \mu \frac{\mathbf{u}(\Delta y)}{\Delta y} \tag{1}$$

with μ representing the dynamic viscosity and the range of Δy limited the viscous layer ($y^+ < 5$). Here it is crucial that the wall distance Δy is corrected for any offset and tilt of the wall surface as described in Sect. 3.

4.1 Error estimation

The estimation of the wall shear stress τ_w based on the discrete approximation given in Eq. 1 is affected by two primary sources of error: (1) the uncertainty of the distance of the particle from the wall ϵ_y and (2) the measurement uncertainty in the particle’s velocity ϵ_u. In combination, the two errors will result in a rapid increase in the measurement uncertainty toward the wall. Classical methods of error propagation provide the relative error of the estimated WSS for the approximation given in Eq. 1:

$$\epsilon_{\tau_w}(y) = \frac{\delta \tau_w}{\tau_w} = \left[\epsilon_u{}^2 + \epsilon_y{}^2\right]^{0.5} \tag{2}$$

$$= \left[\left(\frac{\delta u(y)}{u(y)}\right)^2 + \left(\frac{\delta y}{y}\right)^2\right]^{0.5} \tag{3}$$

Reasonable constraints for δy and $\delta u(y)$ can be derived from the residuals of the three-component reconstruction or the track fitting scheme, here, a cubic B-spline. After validation, the latter are in the order of $r_{\mathrm{fit}} = 5\,\mu\mathrm{m}$ in the sampling domain $[0.5 < y^+ < 1.5]$ (see Fig. 11d). As depicted in Fig 7, the error on a single WSS estimate can be in excess of 10 % in the domain of interest. These estimates are based on the mean residual of the B-spline curve fit, r_{fit}, obtained by subtracting the 3d track particle positions from their fitted positions. Very close to the wall ($y^+ < 2$), the particle motion has a negligible wall-normal component v such that the error can be constrained in the validation step by limiting the variance of v (dash–dot and dotted curves in Fig 7). However, this has only a minor influence on the WSS error ϵ_{τ_w}.

Using the single sample uncertainty $\sigma_{\tau_w} = \epsilon_{\tau_w} \tau_w$, the uncertainty on the mean and higher-order statistics of a quantity x can be expressed in terms of the 95 % confidence interval (Benedict and Gould 1996):

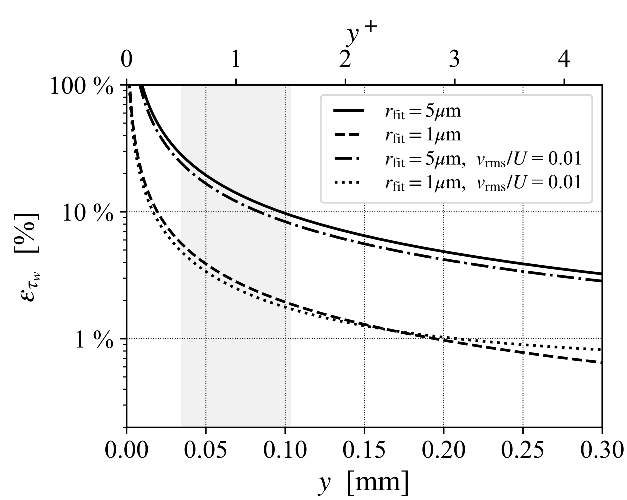

Fig. 7 Estimated error of the WSS for different mean values of the residuals of the 3d cubic B-spline track fitting

$$\epsilon_{\langle x\rangle} = \frac{1.96}{\langle x\rangle}\sqrt{\frac{\sigma_x^2}{N_{s,eff}}} \tag{4}$$

$$\epsilon_{x_{\mathrm{rms}}} = \frac{1.96}{\langle xx\rangle^{0.5}}\sqrt{\frac{\sigma_x^2}{2N_{s,eff}}} \tag{5}$$

where $N_{s,eff} < N_s$ is the estimated number of uncorrelated samples within the set N_s and can be obtained by accounting for the integral time scale T_u for the near-wall flow. Using DNS, Quadrio and Luchini (2003) estimated the integral time sale T_u in the viscous layer at about 20 viscous time scales, $t^* = \nu u_\tau^{-2} \approx \tau_\eta$ (see Eq. 15), such that $T_u \approx 20\,t^* \approx 6\,\mathrm{ms}$ at $U_\infty = 5.2\,\mathrm{m/s}$. This time span covers 30 laser pulses (at $f_s = 5\,\mathrm{kHz}$) such that the effective number of samples becomes:

$$N_{s,eff} = \frac{1}{T_u f_s} N_s = \frac{1}{30} N_s. \tag{6}$$

For $U_\infty = 7.5\,\mathrm{m/s}$ and $U_\infty = 10\,\mathrm{m/s}$, the factor $T_u f_s$, respectively, reduces to 16.4 and 10.0. Combining Eqs. 4 and 5 with Eq. 6 yields the uncertainty estimates for the given quantities. Even with a single sample uncertainty of $\epsilon_x = 20\,\%$, the large sample sizes of $\mathrm{O}(1 \times 10^7)$ reduce the relative uncertainty to levels of $\mathrm{O}(1 \times 10^{-3})$ for the root mean square (rms) values. Here it should be noted that this uncertainty does not include more influential bias errors that are, e.g., introduced by possible misalignment of the estimated wall plane as well as vibrations and other calibration related errors.

Another source of uncertainty is routed in the linearity assumption of the fluid velocity within the viscous sublayer. As illustrated in Fig. 8c for direct numerical simulation (DNS) TBL, the profile of mean streamwise velocity already deviates by nearly 4 % from linearity at a wall distance of $y^+ = 5$. Therefore, a reliable estimation relies on particle velocity data provided for $y^+ \leq 4$. At the same time, the relative uncertainty of y_p rapidly increases as the particle distance Δy approaches the wall as described before.

The availability of DNS also provides justification for track validation based on the variances of the individual velocity components along the track. In particular, Fig. 8e shows that at a wall distance of $y^+ < 2$, the wall-normal fluctuations v_rms are an order of magnitude smaller than streamwise or spanwise fluctuations. More importantly, the velocity fluctuations, shown in Fig. 8f, converge differently toward their limiting values at the wall, which has a notable influence on the estimation of the WSS fluctuations as described later.

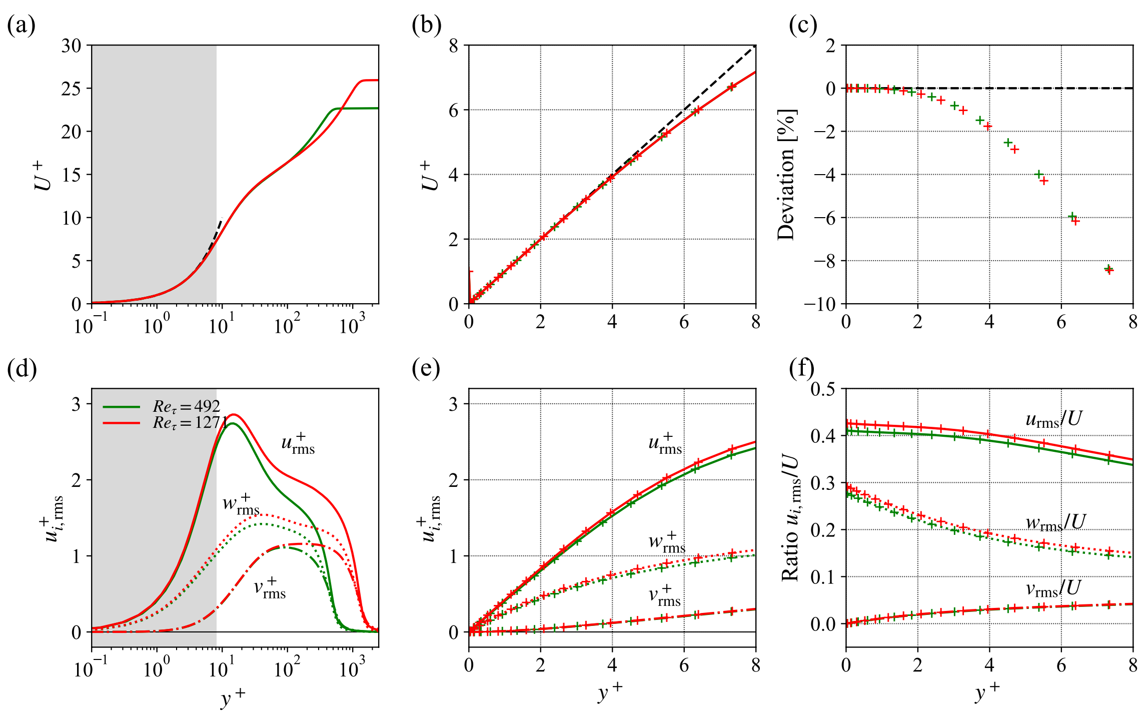

Fig. 8 Profiles of mean streamwise U^+ (top row) and root mean square (rms) of all three velocity components (bottom row) from DNS of TBLs by Sillero et al. (2013) in log-scaling (**a**,**d**), linear scaling near the wall (**b**,**d**). (**c**): deviation of U^+ from linearity; (**f**): velocity root mean square (rms) normalized with U^+. Gray shaded areas in (**a**,**d**) represent domains in (**b**,**c**,**e**,**f**) for $y^+ \leq 8$

5 Results

Figure 9 shows two realizations of recovered near-wall tracks at $U_\infty = 5.2\,\mathrm{m/s}$ ($\mathrm{Re}_\tau = 563$). The particle positions are color coded with the local wall stress magnitude $|\,\vec{\tau}_w\,|$. While the tracks in Fig. 9a indicate a low-shear condition and even some flow reversal, the flow topology is completely different only 8 ms later (Fig. 9b) when it is dominated by a high shear rate aligned with the mean flow direction. The shear rate partially exceeds the mean value by a factor of two. Animations of the near-wall particle motion at different playback speeds are provided as part of the supplementary material, see section Appendix 2.

A short record of 0.2 s duration shows the evolution of WSS estimates within a small ($1 \times 1\,\mathrm{mm}^2$) area in Fig. 10. The streamwise component τ_x reaches negative values (reverse flow, marked red in plot) at $t \approx 13.93$ s and $t \approx 13.98$ s, whereas the spanwise component τ_z exhibits several extreme events in excess of 3-4 times the rms. Of importance is the fact that the randomness of the LPT data does not provide continuous time records for a given point. This prevents the ad hoc calculation of space–time characteristics such as frequency spectra or temporal correlations. To allow this, the random data would first need to be subjected to data assimilation or interpolation schemes.

5.1 Mean velocity profile and statistics

Profiles of mean particle velocity and associated higher moments are compiled by bin-averaging across the FOV at different discrete wall distances y_i of sample height Δy. Figure 11 presents profiles obtained with a bin height of $\Delta y = 1\,\mu\mathrm{m}$. The mean streamwise profile (Fig. 11a) is in good agreement with the DNS up to a wall distance of $y \approx 200\,\mu\mathrm{m}$ beyond which it begins to deviate. The deviation is believed to be sourced in the under-representation of faster particle tracks in the statistics: at a velocity of $U = 1\,\mathrm{m/s}$ the particles move 20 pixel between laser shots, such that faster moving particles are less likely to be tracked reliably. This could be improved by increasing the laser pulsing frequency,

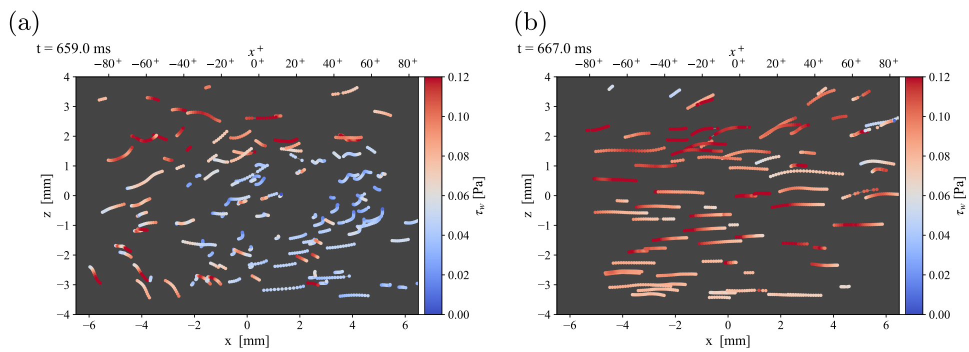

Fig. 9 Processed particle tracks color coded with wall shear stress magnitude at $\mathrm{Re}_\tau = 563$ ($U_\infty = 5.2\,\mathrm{m/s}$). Each frame represents 5 ms of event data (25 light pulses). The mean flow direction is from left to right. The time separation between frame (**a**) and frame (**b**) is 8 ms

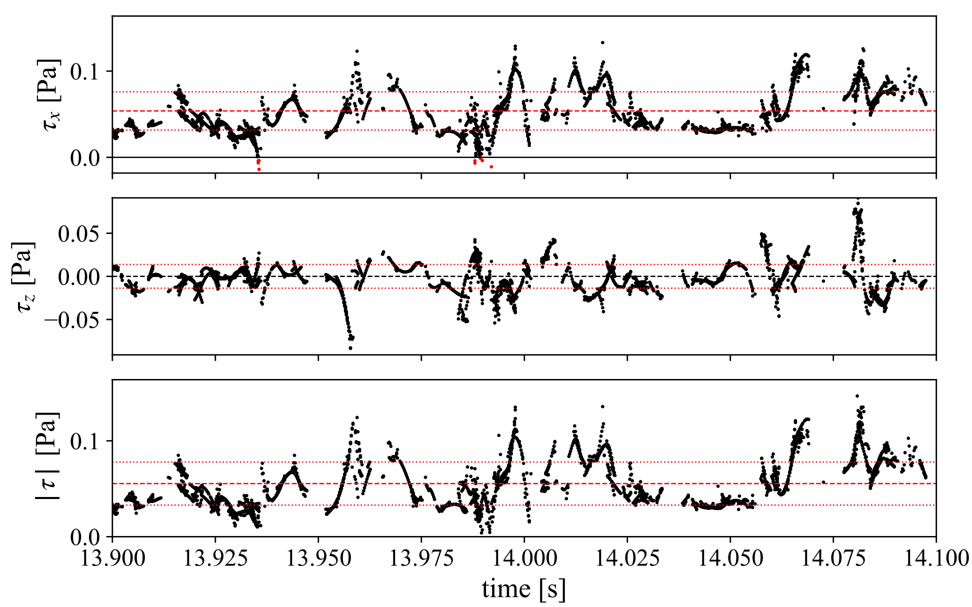

Fig. 10 0.2 s sample of WSS data at $\mathrm{Re}_\tau = 563$ ($U_\infty = 5.2\,\mathrm{m/s}$) sampled in an area of $1 \times 1\,\mathrm{mm}^2$, streamwise (top), spanwise (middle) and magnitude (bottom). Dashed lines indicate mean of quantity, dotted lines ± 1 standard deviation (rms)

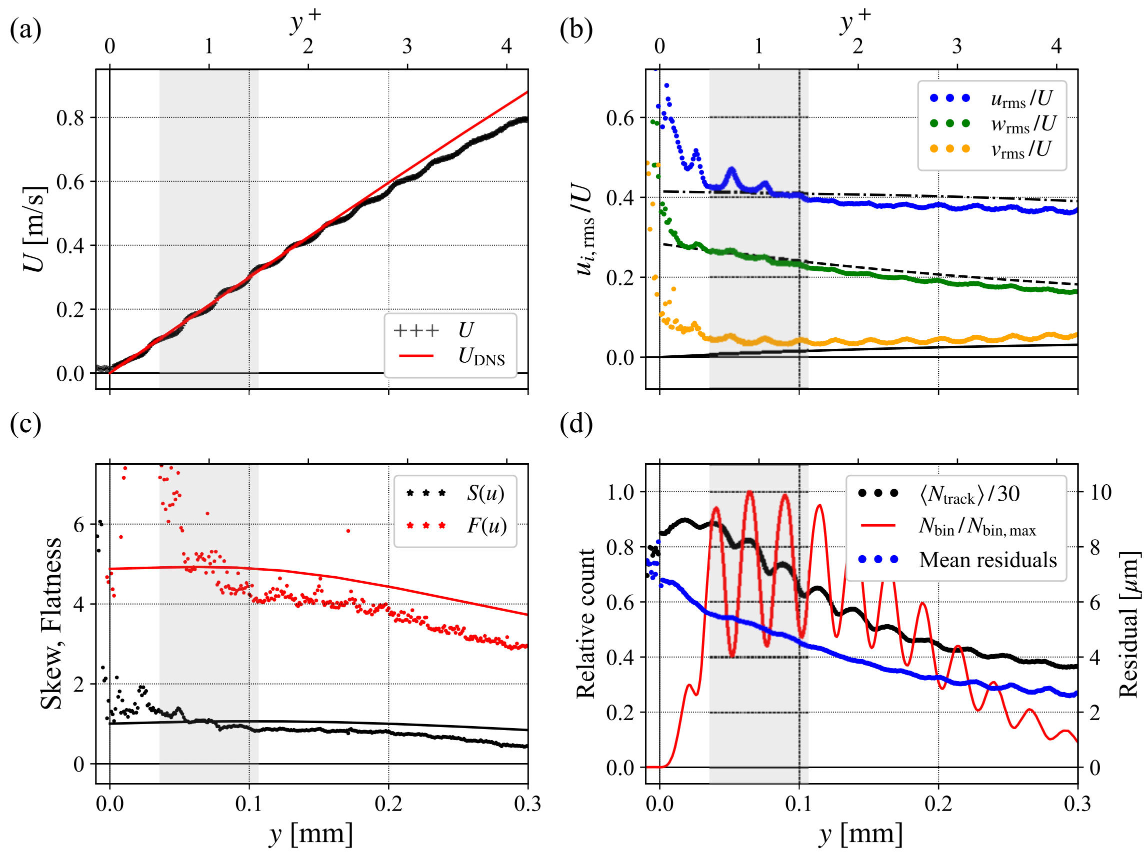

Fig. 11 Bin-averaging results using bins of $\Delta y = 1\,\mu\mathrm{m}$: (**a**) near-wall velocity profile (+) and DNS prediction (red line), gray area indicates sampling domain for WSS estimation; (**b**) rms of velocity components for streamwise (blue), spanwise (green) and wall-normal (gray) components; (**c**) skewness $S(u)$ and flatness $F(u)$ estimates of streamwise velocity in comparison to values predicted by DNS (solid lines, from Schlatter and Örlü 2010); (**d**) relative sample count N_{bin} within the bins (red line) and averaged track length normalized by maximum possible ($N_{\max} = 30$)

but must be balanced against a reduced number of tracks in order not to exceed the limited event detection rate of the EBV sensor. In addition, a latency of $\approx 100\,\mu\mathrm{s}$ of the used EBV cameras restricts pulsing rates to below $\approx 10\,\mathrm{kHz}$ to prevent cross-talk between adjacent light pulses. For the present data set, useful velocities are available up to a wall distance of $y^+ \approx 4$ ($300\,\mu\mathrm{m}$). For the estimation of WSS, the sampling volume is restricted to one viscous unit with the range $[0.5 < y^+ < 1.5]$.

The slope of the mean profile in a range $[20\,\mu\mathrm{m} \leq y \leq 150\,\mu\mathrm{m}]$ is used for the estimation of the mean velocity gradient at the wall, $\partial u/\partial y|_{y=0}$, which in turn is required in (Eq. 1) to estimate the mean WSS, $\langle \tau_w \rangle$, alongside with the estimation of the viscous scaling $l^* = \nu/u_\tau$.

The rms of all three components of the particle velocity is plotted in Fig. 11b and is in reasonable agreement with DNS following the trend but slightly underestimates the DNS reference. The rms of the wall-normal component v_{rms} is at a nearly constant level throughout, indicating noise. With the near-wall flow essentially restricted to be only wall parallel, track validation can rely on limiting the variance and magnitude of the wall-normal component (see also Fig. 8f).

Finally, Fig. 11c provides the third and fourth order moments, that is, skewness $S(u)$ and flatness $F(u)$ of the streamwise velocity. While also underestimating the DNS predictions, the profiles begin to strongly deviate with increased proximity to the wall, indicating an increased amount of erroneous data near the wall, the net effect of which is averaged out in both the mean and the rms fluctuations.

In addition to the profiles of mean and higher-order moments, Fig. 11d provides the relative sample count for each of the $1\,\mu\mathrm{m}$ bins (black line). This value modulates at a spatial frequency of $\Lambda = 24.0 \pm 0.5\,\mu\mathrm{m}$ and can be explained by an intensity modulation within the laser light sheet that is reflected by the glass surface while grazing it at a shallow angle. Within the darker regions, the probability of event

Table 2 Statistics of the WSS for different data sets sampled at a wall distance $[0.5 < y^+ < 1.5]$. Estimated values for $\tau^+_{i,\mathrm{rms}}$ according to Eq. 8

U_∞ [m/s]	**5.2**			**7.5**			**10.0**
Re_τ	**563**			**754**			**935**
Data set	5-3	5-1	5-4	7-1	7-2	7-3	10-1
$\tau^+_{x,\mathrm{rms}}$ (est.)		0.412			0.417		0.421
$\tau^+_{x,\mathrm{rms}}$	0.413	0.416	0.415	0.417	0.427	0.428	0.439
diff	+0.2 %	+1.2 %	+0.7 %	±0 %	+2.3 %	+2.6 %	+4.3 %
$\tau^+_{z,\mathrm{rms}}$ (est.)		0.278			0.283		0.287
$\tau^+_{z,\mathrm{rms}}$	0.243	0.244	0.240	0.235	0.237	0.237	0.229
diff	−12.6 %	−12.2 %	−13.7 %	−17.0 %	−16.2 %	−16.2 %	−20.2 %
$S(\tau_x)$	0.978	1.012	1.027	0.989	0.997	0.992	0.942
$S(\tau_z)$	0.028	0.010	− 0.023	0.007	− 0.005	0.040	− 0.001
$F(\tau_x)$	4.41	4.56	4.66	4.45	4.60	4.56	4.45
$F(\tau_z)$	6.76	7.39	7.77	7.43	7.83	8.19	7.20
N_s	11×10^6	32×10^6	26×10^6	3.7×10^6	3.7×10^6	4.2×10^6	3.8×10^6
$N_{s,eff}$	0.3×10^6	1×10^6	0.9×10^6	0.2×10^6	0.2×10^6	0.3×10^6	0.4×10^6

generation is reduced which results in a local reduction in track data rate. The spacing of the interference fringes, Λ, is related to the incidence angle θ by

$$\Lambda = \frac{\lambda}{2\sin(\theta)} \tag{7}$$

where λ is the wavelength of the laser light (i.e., 532 nm). The estimated angle of $\theta = 0.635\,°$ matches the 5 mm entry height of the laser beam 500 mm away at the side of the tunnel.

The interference pattern introduces modulation in the velocity profiles and associated higher moments that become more pronounced with closer proximity to the wall. The influence of the light intensity modulation on event generation and resulting biased 3d particle positions is not yet fully understood. A possible explanation could be a proportionally higher number of single-pixel-sized particle images in the intensity minima which have a higher reconstruction 3d uncertainty compared to larger particle images observed in the brighter regions. The smaller particle images have a higher 3d reconstruction uncertainty and are likely to be position biased in a manner similar to the pixel-locking effect in PIV. Ideally, this interference borne data modulation should have been prevented altogether, such as by placing a non-reflective coating just outside of the immediate field of view. In light of this, the fluctuations $u_{i,\mathrm{rms}}$ have their highest deviations from the predicted profiles at the minimum sample count which suggests that the most reliable values are located at the maxima of the sample counts. It should be noted that these modulations would not have been detected without an accurate plane adjustment as part of the camera calibration (cf. Figure 5b).

5.2 Wall shear stress distribution and statistics

Following Eq. 1, the unsteady wall shear stress (WSS) estimates are directly calculated using the particle's current velocity u_i and distance from the wall Δy_i. Probability distributions of both components of the WSS vector are given in Fig. 12 for $U_\infty = 5.2$ m/s and Fig. 13 for $U_\infty = 7.5$ m/s. The distributions closely match those found

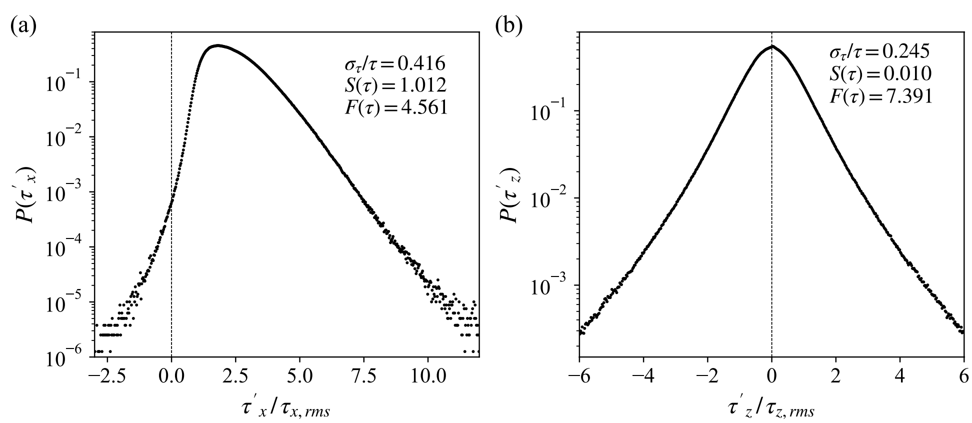

Fig. 12 PDFs of streamwise (**a**) and spanwise (**b**) wall shear stress components normalized by the rms of the respective values compiled from $N_s = 30 \times 10^6$ correlated samples obtained from an event record of 60 s duration at $U_\infty = 5.2$ m/s ($\mathrm{Re}_\tau = 563$). Velocity data are sampled in the range $[0.5 < y^+ < 1.5]$ using particle tracks with a minimal length of 7

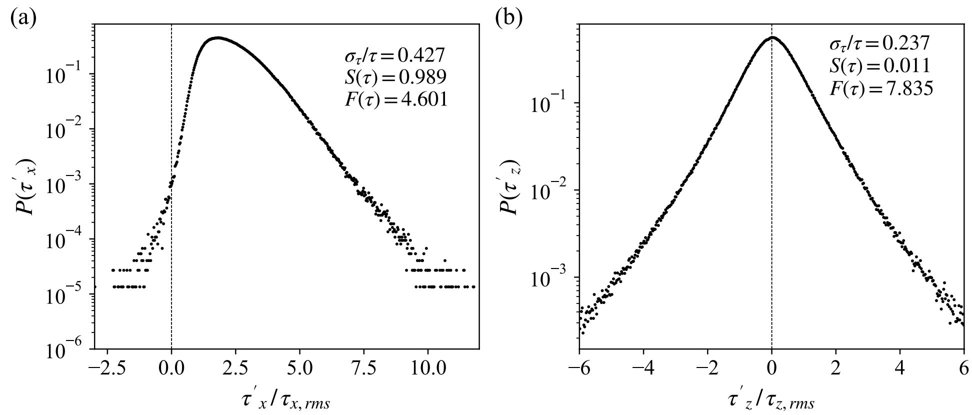

Fig. 13 Same as Fig. 12 obtained at $U_\infty = 7.5$ m/s ($\mathrm{Re}_\tau = 754$) using 10 s of data with $N_s = 4.2 \times 10^6$

in literature for DNS data (e.g., Figure 5 in Diaz-Daniel et al. 2017) and experiments (e.g., Figure 7 in Liu et al. 2019). At $U_\infty = 5.2$ m/s, the data set is based on a 60 s record and sampled in a wall distance of $[0.5 < y^+ < 1.5]$ ($y = 35 \sim 105$ μm) for the estimation of the WSS according to Eq. 1. For 60 s of processed event data, the statistics represent a total of 8000 boundary layer turnover times of $\delta_{99}/U_e = 5.2$ ms ($\mathrm{Re}_\tau = 563$, $\delta_{99} = 39$ mm).

The skewness S_{τ_x} and flatness F_{τ_x} of the WSS components, summarized in Table 2, are in good agreement with data obtained at similar Reynolds numbers from DNS and experiments alike (see, e.g., Table I in Diaz-Daniel et al. 2017).

The correlations for the rms of the WSS, $\tau^+_{x_i,rms}$, proposed by Örlü and Schlatter (2011) have a Reynolds number dependency:

$$\tau^+_{x_i,\mathrm{rms}} = \frac{\tau_{x_i,\mathrm{rms}}}{\tau_w} = C_{0,i} + 0.018 \ln \mathrm{Re}_\tau \tag{8}$$

with $C_{0,x} = 0.298$ and $C_{0,z} = 0.164$. At $\mathrm{Re}_\tau = 563$, this, respectively, predicts $\tau^+_{x,rms} = 0.412$ and $\tau^+_{z,rms} = 0.278$.

The WSS fluctuation estimates presented in Fig. 14 are compiled from a variety of recordings at different seeding concentrations and different sampling intervals. Whereas the streamwise WSS fluctuations $\tau^+_{x,rms}$ are slightly overestimated, but within error bounds, the spanwise fluctuations $\tau^+_{z,rms}$ are underestimated by more than 10 % which has also been observed in comparable measurements using MAμPTV (Klinner and Willert 2024). A plausible explanation for this underestimation is the different convergence of the velocity fluctuations toward their limiting values at the wall as mentioned in Sect. 4.1 (see Fig. 8f).

Joint probability distributions of the WSS are plotted in Fig. 15 for two Reynolds numbers using a sample size of up to $N_s = 30 \times 10^6$ (at $\mathrm{Re}_\tau = 563$). These distributions agree very well with the results obtained with MAμPTV at the same Reynolds numbers (see Klinner and Willert 2024). Similar data have also been acquired by Sheng et al. (2008)

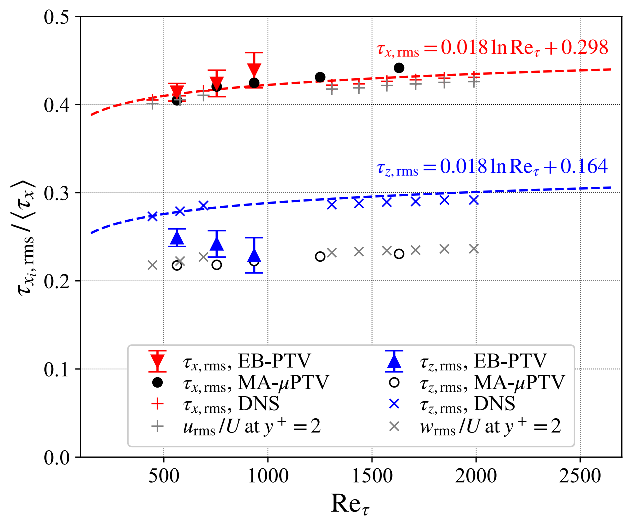

Fig. 14 rms fluctuations of WSS of streamwise (▼) and spanwise (▲) components of the WSS, determined from particle tracks in the viscous sub-layer for $[0.5 < y^+ < 1.5]$. Round markers (•, ∘) represent data obtained with MA-μPTV (Klinner and Willert 2024); TBL-DNS (+, ×) by Sillero et al. (2013). Dashed lines correspond to Eq. 8 with different offsets C_i

for turbulent channel water flow at a friction Reynolds number of $\mathrm{Re}_\tau = 1400$ ($u_\tau = 0.056$ m/s) and by Bross et al. (2019) for a TBL in air at $\mathrm{Re}_\tau = 2500$ ($u_\tau = 0.191$ m/s).

The contours in Fig. 15b show a small bulge near $\tau_w = 0$ which is believed to be caused by artifacts arising by the colinear arrangement of the three cameras along the streamwise direction. Due to this linear camera arrangement, the epipolars between all three cameras are parallel. Therefore, multiple particles moving in streamwise direction have a higher likelihood of overlapping along the field of view and result in mismatching (ghost particles). This effect increases as the seeding density is increased. More sophisticated LPT schemes, such as a modified 3d STB (Schanz et al. 2016), should be able to handle this deficiency and could

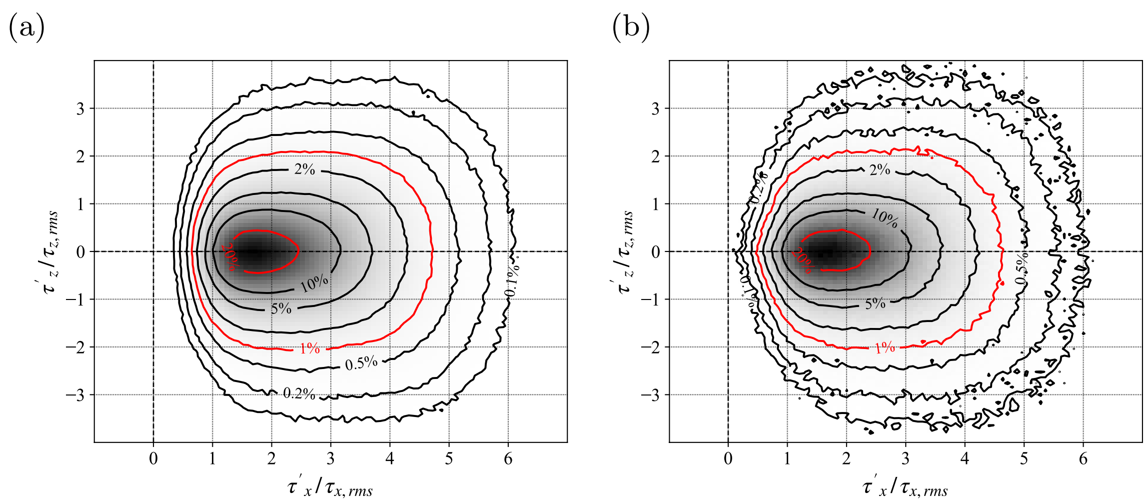

Fig. 15 Joint PDFs of the wall shear stress vector normalized by the rms of the respective components obtained at $U_\infty = 5.2$ m/s ($\mathrm{Re}_\tau = 563$, (**a**)) and $U_\infty = 7.5$ m/s, ($\mathrm{Re}_\tau = 754$, (**b**)). Contour levels represent probabilities of 0.1%, 0.2%, 0.5%, 1% (red), 2%, 5%, 10%, 20% (red)

potentially recover more tracks from the raw event data. Adding a fourth camera would also reduce the likelihood of particle mismatch.

5.3 WSS rate of change

Visualizations of the particle motion within the viscous sublayer exhibit strong spanwise activity that give an impression that the spanwise unsteadiness is more pronounced and of higher amplitude than the streamwise fluctuations (see, e.g., video supplement, Sec. B). To address this, we extracted the rate of change of the WSS from the particle tracking data as part of the B-spline track fitting step. Following the procedure of determining the unsteady WSS vector from the near-wall velocity data as per Eq. 1, the particle acceleration vector $\mathbf{a_p} = [a_{p,x}, a_{p,y}, a_{p,z}]$ can be retrieved from the tracking data and is related to the rate of change of the WSS vector:

$$\frac{\partial}{\partial t}(\vec{\tau}_w) = \frac{\partial}{\partial t}\left(\mu \frac{\partial \mathbf{u}}{\partial y}\bigg|_{y=0}\right) = \mu \frac{\partial \mathbf{a}}{\partial y}\bigg|_{y=0} \approx \mu \frac{\mathbf{a_p}(\Delta y)}{\Delta y}. \tag{9}$$

In the following, the symbol $\hat{a}$ refers to this quantity and in effect is the particle acceleration $a_{p,i}$ divided by the wall distance:

$$\hat{a}_i = \frac{\partial \tau_i}{\partial t} = \lim_{y\to 0} \frac{a_{p,i}}{y} \tag{10}$$

Similar to the wall-normal velocity component v, the wall-normal acceleration a_y also vanishes due to the no-slip boundary condition at the wall.

Figure 16 presents probability density functions (PDFs) of the rate of change of the WSS, $\hat{a}$, for both streamwise and spanwise directions with a joint PDF of the data shown in Fig. 17. Noteworthy is the near perfect symmetry of the distributions with a slight shift of the streamwise component toward negative values (deceleration). This may be explained by the deceleration of the fluid within the boundary layer in the presence of a slightly positive pressure gradient. The rms of the WSS rate of change $\hat{a}$ is also essentially equivalent for both components, deviating by less than 5 % (cf. Table 3).

Distributions of the near-wall particle acceleration and its relation to the WSS rate of change are rarely reported in the literature and mostly discussed in the context of inertial particle transport using DNS. The PDFs shown in Fig. 16 are strongly non-Gaussian and exhibit strongly pronounced tails with a high flatness $F(\hat{a}) = 30 \sim 50$, which is indicative of high intermittency. This was already observed by, e.g., Yeo et al. (2010) for TCFs with $\mathrm{Re}_\tau = 180 \sim 600$. The distributions in Fig. 16 have a strong resemblance to acceleration data obtained from both DNS and experiments (by LPT) for inertial particles in homogeneous and isotropic turbulence (HIT) (Voth et al. 2002; Mordant et al. 2004; Schröder et al. 2022). In this context, a stretched exponential function, also known as log-normal superstatistics (Beck 2004), is generally used to describe the shape of the probability distribution with Stelzenmuller et al. (2017) proposing the following expression:

$$p(\hat{a}_i) = \frac{e^{s_i^2/2}}{4m_i}\left[1 - \mathrm{erf}\left(\frac{\ln \frac{|\hat{a}_i|}{m_i} + s_i^2}{\sqrt{2}\, s_i}\right)\right]. \tag{11}$$

According to (Stelzenmuller et al. 2017), the parametric variable s_i defines the shape of the distribution, whereas m_i is related to the variance of a_i. For the present WSS rate of change data, nonlinear least squares fitting yields $s = 0.785 \pm 0.014$ and $m = 0.941 \pm 0.026$ and an estimated flatness in the range of $30 \sim 40$ (c.f. Table 3). Although the

Table 3 Statistics of the WSS rate of change $\hat{a}_i = \partial\tau_i / \partial t$ for different data sets sampled at a wall distance $[0.5 < y^+ < 1.5]$. Values for "LN-fit" are obtained from nonlinear least squares fit of Eq. 11

U_∞, [m/s]	**5.2**			**7.5**			**10.0**
Re_τ	**563**			**754S**			**935**
Data set	5-3	5-1	5-4	7-1	7-2	7-3	10.1
$\langle\hat{a}_x\rangle$, [Pa/s]	− 0.849	− 0.866	− 0.900	− 3.055	− 2.901	− 2.979	− 6.227
$\langle\hat{a}_z\rangle$, [Pa/s]	− 0.018	− 0.006	− 0.005	0.001	− 0.032	0.023	− 0.006
$\hat{a}_{x,\mathrm{rms}}$, [Pa/s]	11.42	10.92	11.32	34.47	33.82	34.02	75.44
$\hat{a}_{x,\mathrm{rms}}$, [Pa/s]	11.17	10.83	10.96	34.18	34.15	34.47	72.93
$\frac{\hat{a}_{z,\mathrm{rms}}}{\hat{a}_{x,\mathrm{rms}}}$	0.978	0.976	0.968	0.991	0.976	1.01	0.967
$S(\hat{a}_x)$	− 0.628	− 0.883	− 0.862	0.600	− 0.110	− 0.275	− 0.184
$S(\hat{a}_z)$	− 0.024	0.009	− 0.056	0.060	0.275	− 0.000	0.219
$F(\hat{a}_x)$	49.4	58.5	58.2	65.3	28.3	47.7	27.5
$F(\hat{a}_z)$	32.8	29.9	51.5	35.5	75.1	31.8	74.1
$F(\hat{a}_x)$ (LN-fit)	32.7	33.5	33.9	34.9	34.6	34.7	35.4
$F(\hat{a}_z)$ (LN-fit)	34.7	35.9	37.1	41.9	41.4	42.1	46.8
s_x (LN-fit)	0.770	0.772	0.782	0.807	0.802	0.802	0.829
s_z (LN-fit)	0.782	0.791	0.811	0.848	0.849	0.853	0.921
m_x (LN-fit)	0.977	0.959	0.956	0.954	0.959	0.959	0.964
m_z (LN-fit)	0.936	0.913	0.904	0.848	0.848	0.836	0.819

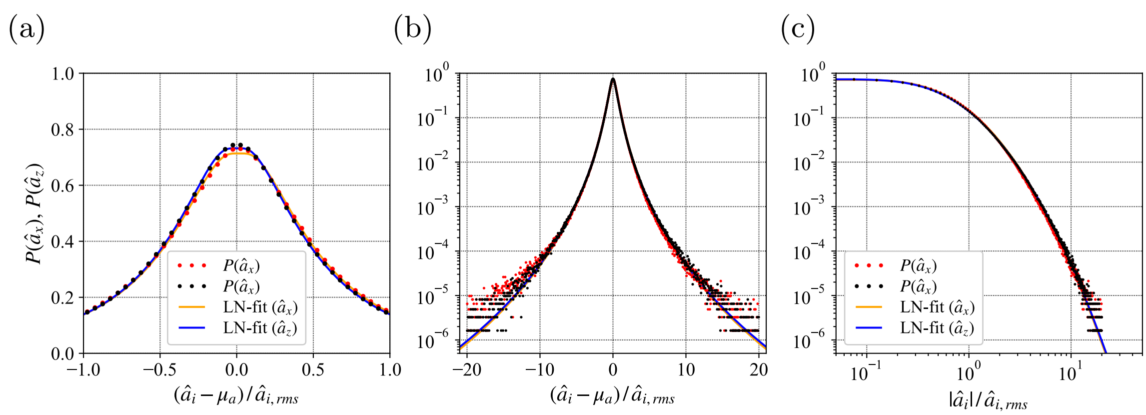

Fig. 16 PDFs of rate of change of the WSS components normalized by the rms of the respective values compiled from $N_s \approx 30 \times 10^6$ samples at $U_\infty = 5.2\,\mathrm{m/s}$ ($\mathrm{Re}_\tau = 563$). Data are sampled in the range $[0.5 < y^+ < 1.5]$ using minimal track length of $N_{\mathrm{track}} = 7$. Detail near peak in linear scaling (**a**), logarithmic scaling (**b**), double-log scaling (**c**). Solid lines represent a stretched exponential fit according to Eq. 11

investigated near-wall flow is very anisotropic by nature, the striking similarity of the PDFs $P(\hat{a})$ to those of HIT could indicate a certain universality as already pointed out by (Stelzenmuller et al. 2017). Whereas previous studies have noted increased asymmetric PDFs of the acceleration components with increased proximity to the wall (e.g., Stelzenmuller et al. 2017, Zamansky et al. 2011, Yeo et al. 2010), there is little information on the limiting case of particle acceleration very close to the wall ($y^+ < 2$ in present experiments), in particular the rate of change of the WSS, $\hat{a}$, determined from the particle acceleration (see Eq. 9). Our findings suggest a fully symmetric (isotropic) behavior of the wall shear stress rate of change.

5.4 Two-point correlations of WSS

Two-point correlations provide a measure of similarity between the data u_1 at a given point $\mathbf{x}_0$ in space $\mathbf{x}$ (or time t) with respect to the data point u_2 in its neighborhood. Here it is calculated for the two wall shear stress components $\tau_i = \tau_i\ (x,\ y,\ z,\ t)$ using the discrete version of the cross-correlation coefficient:

$$R_{\tau_i\tau_j}(\mathbf{x},\mathbf{x}_0) = \frac{\int \tau_i'(\mathbf{x},t)\,\tau_j'(\mathbf{x}_0,t)\,dt}{\sqrt{\int \tau_i'(\mathbf{x},t)\,\tau_i'(\mathbf{x},t)\,dt} \cdot \sqrt{\int u_j'(\mathbf{x}_0,t)\,\tau_j'(\mathbf{x}_0,t)\,dt}} \tag{12}$$

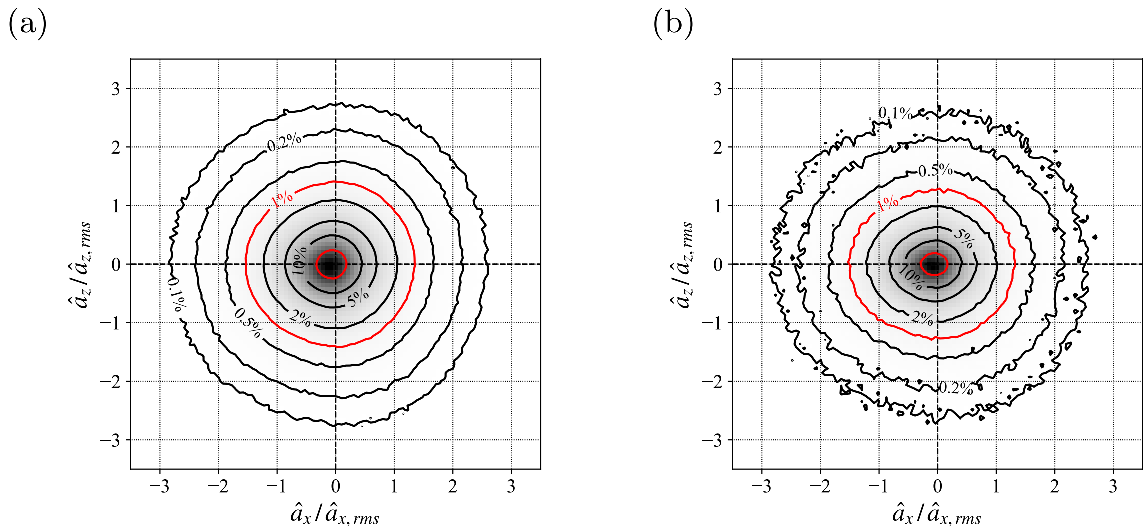

Fig. 17 Joint PDFs of the wall shear stress rate of change normalized by the rms of the respective components obtained at $U_\infty = 5.2\,\mathrm{m/s}$ ($\mathrm{Re}_\tau = 563$, (**a**)) and $U_\infty = 7.5\,\mathrm{m/s}$ ($\mathrm{Re}_\tau = 754$, (**b**)). Contour levels represent probabilities of 0.1%, 0.2%, 0.5%, 1% (red), 2%, 5%, 10%, 20% (red)

$$=\frac{\langle\, \tau_i'(\mathbf{x},t)\cdot \tau_j'(\mathbf{x}_0,t)\,\rangle}{\langle \tau_i'(\mathbf{x},t)^2\rangle^{0.5}\cdot\langle \tau_j'(\mathbf{x}_0,t)^2\rangle^{0.5}} \tag{13}$$

where the two quantities in the denominator are the square roots of the sample variances (i.e rms of τ_k) while y is held constant (i.e. near-wall plane, $y^+ = 1$). With the present WSS data being ungridded, the calculation of Eq. 13 requires a bin-averaging approach. Furthermore, it is assumed that the flow statistics are constant across the field of view such that each sampled value at position $\mathbf{x}_0$ is assumed to be located at the origin ($x = 0, z = 0$). The distance to other points in the sample defines the location of the bin for incremental accumulation of the correlation statistics. As a result, the effective size of the correlation map is larger than the data domain, with decreasing bin entries toward the edges.

For the present data set, a square bin size of $\Delta x \times \Delta z = 250 \times 250\,\mu\mathrm{m}^2$ ($3.6\,x^+ \times 3.6\,z^+$) was chosen. As in the previous data processing, the data are sampled from a volume of one viscous height $[0.5 < y^+ < 1.5]$ resulting in a sample size of $N_s \approx 30 \times 10^6$.

The two-point correlation maps provided in Fig. 18a–c agree with DNS-based results by Jeon et al. (1999) for $\mathrm{Re}_\tau = 180$ with deviations most likely related to the difference in Reynolds number (see Figs. 7a,b and 8a in their paper). Recent 3d-STB data by Schröder et al. (2024) obtained from the same wind tunnel facility yielded very similar two-point correlation maps, albeit the sampling plane being located at $y^+ = 5$.

The elongated contours of $R_{\tau_x\tau_x}$ are related to the streamwise near-wall streaks—wall parallel, counter-rotating vortical structures aligned in streamwise direction. Along $x = 0$, the minima are, respectively, located at $\pm 58\,z^+$ for $R_{\tau_x\tau_x}$ and $\pm 47\,z^+$ for $R_{\tau_z\tau_z}$ which corresponds to the mean spanwise spacing of about $100 \sim 120$ viscous units reported in the literature (Smith and Metzler 1983 and others). The correlation map for $R_{\tau_x\tau_z}$ shows a double-peak feature inclined at $\approx \pm 5^\circ$ that relates the streamwise WSS τ_x to an off-axis maximum spanwise τ_z about $70 \sim 80\,x^+$ further downstream. This topology is likely to be related the $\approx \pm 6^\circ$ features observed in space-time correlations by Lagraa et al. (2004), although this needs further investigation.

Compared to the correlation maps of WSS, the spatial signature of the WSS rate of change, $\hat{a}$, shown in Fig. 18d–f, is much more compact with lobe-like negative correlation features. Very similar topology has been reported by Schröder et al. (2024) (see Fig. 11 in their publication). The fluid dynamical processes associated with the correlation topologies have yet to be investigated in further detail, and literature on this particular aspect is not known to the authors.

6 Discussion

In the course of the experiments, event data were collected at different seeding densities to assess its influence while keeping all other parameters constant. The track detection rate given in Table 1 indicates that there is an optimum event data rate of about 8–12×10^6 Ev/s. A further increase in the event rate (= higher seeding) actually results in a reduction in the track detection rate. With increased particle image density, the likelihood of particle ambiguity and false track initialization also increases. At the highest seeding level with

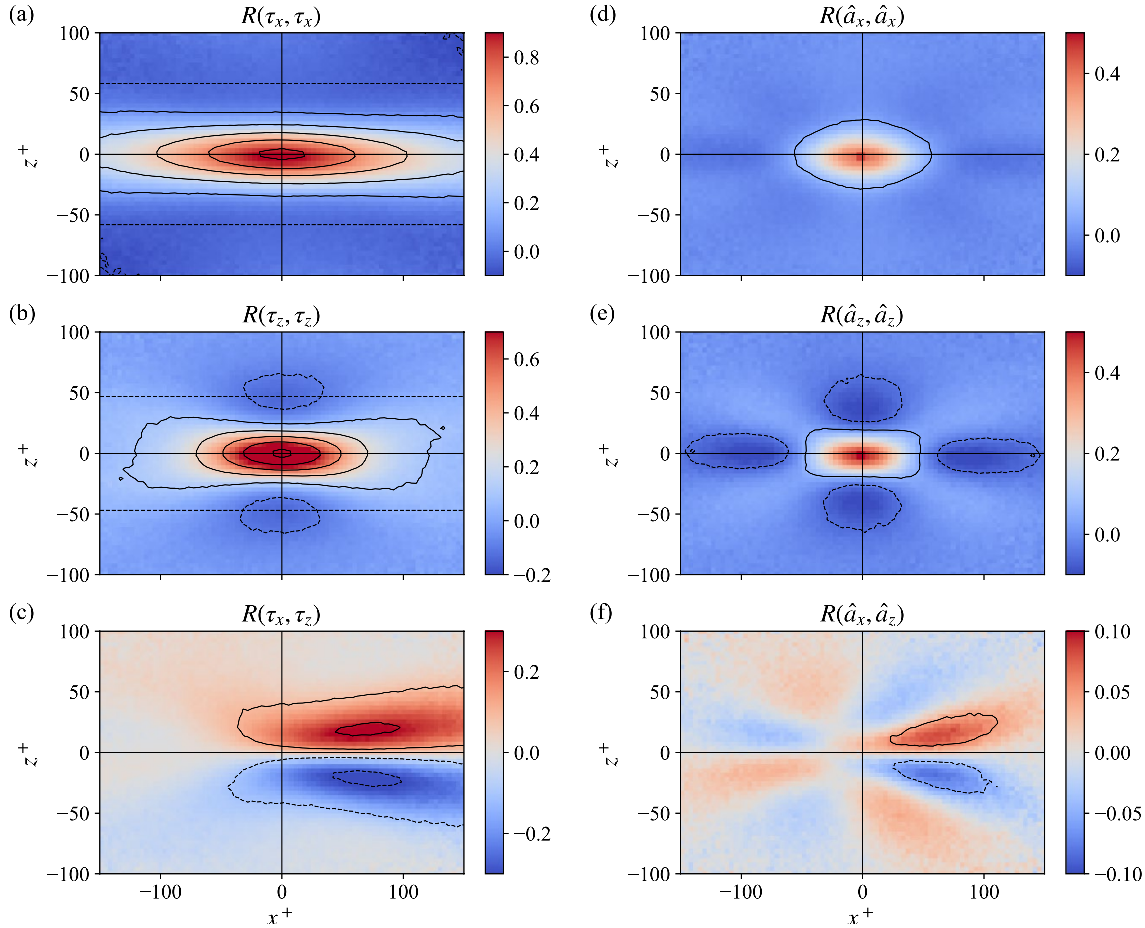

Fig. 18 Two-point correlation maps of the WSS (**a–c**) and its rate of change $\hat{\mathbf{a}}$ (**d–f**) obtained at $U_\infty = 5.2\,\mathrm{m/s}$ ($\mathrm{Re}_\tau = 563$) using tracking results from $[0.5 < y^+ < 1.5]$ and sample size of $N_s \approx 30 \times 10^6$. Contour lines at -0.1, $+0.1$, $+0.3$ ⋯ (left column), ± 0.05 (right column). Horizontal dashed lines indicate position of minima along $x = 0$

more than 20×10^6 Ev/s (data set 5–2), the valid track validation rate drops to less than 5 %, which is why this data set was omitted in the data analysis. Here an approach that first reconstructs the 3d particle positions followed by 3d track building, rather than tracking in 2d space for each camera view, is likely to provide better results.

Along with the increase in event rate, the saturation of the sensor readout causes increased latency in the time stamping such that pulses are no longer clearly separated; derived pseudo-frames will contain particle images from more than one pulse which cannot be separated in time. This also impacts the particle tracking performance.

Even at optimal particle image density and event data rate, the WSS determined from the tracking results showed a consistent underestimation of the spanwise WSS fluctuation $\tau^+_{z,rms}$. This was also found in related measurements using highly accurate microparticle tracking techniques by Kumar et al. (2021) and Klinner and Willert (2024). Here DNS is particularly helpful in explaining the underestimation: Fig. 8d provides profiles of the velocity fluctuations for all 3 velocity components. Focusing in on the near-wall region ($y^+ < 8$) in Fig. 8e, they are characterized by different rates of change, with u^+_{rms} to strongest, followed by spanwise w^+_{rms} ($\approx$ 40% at $y^+ = 5$) and wall-normal v^+_{rms} ($\approx$ 10% at $y^+ = 5$). However, when these quantities are normalized with the mean streamwise velocity $U(y)$ as shown in Fig. 8f, they exhibit a completely different behavior: while the quantity u_{rms}/U shows gradual decrease, its spanwise counterpart w_{rms}/U rapidly decreases with increasing wall distances, whereas the wall-normal quantity gradually increases from zero at the wall. The limiting values of the former two quantities, u_{rms}/U and w_{rms}/U, at the wall ($y = 0$), in fact, coincide with the WSS fluctuations and represent the DNS-based estimates in Fig. 14. In the context of velocimetry-based WSS estimation, the velocity must be sampled at a finite distance Δy from the wall. Close to the wall, both the velocity and wall distance approach zero and relative errors rapidly increase as explained in Sect. 4.1. Since the quantity u_{rms}/U has a weaker decay compared to w_{rms}/U, the latter will always be underestimated to a much higher degree. This is illustrated in Fig. 14 by sampling the DNS data at a finite wall distance of $y^+ = 2$ as indicated by the gray symbols. This sampling domain is comparable to that chosen for the WSS estimation in the present work and leads to a comparable underestimation of the spanwise WSS fluctuation $\tau^+_{z,rms}$. In principle, the underestimation can be corrected by computing the velocity variances at different wall distance intervals and extrapolating the trend toward the wall. The velocity fluctuations plotted in Fig. 11b closely follow the DNS predictions and justify the extrapolation approach.

At the highest bulk velocity of $U_\infty = 10\,\mathrm{m/s}$, the particle track yield was insufficient for reliable WSS estimation, in part, due to the nearly doubled mean particle displacement (compared to $U_\infty = 5.2\,\mathrm{m/s}$), but also because of the proportional reduction in the viscous scale from $\nu/u_\tau = 69\,\mu\mathrm{m}$ to $\nu/u_\tau = 37\,\mu\mathrm{m}$. To a certain extent, a proportionally higher laser pulsing frequency could improve the measurement. However, the bandwidth limitation of the EBV camera hardware imposes a limit of about 10 kHz, in particular, at increased seeding levels. Overall it was found that the data quality improves with reduced seeding density which is related to the improved particle matching using only three cameras. Adding a fourth camera in the setup would provide additional redundancy, stabilizing the 3d particle position reconstruction.

In terms of FOV and spatial resolution, the herein introduced configuration has advantages over other WSS measurement techniques reported in the literature. Covering an area of $12 \times 7.5\,\mathrm{mm}^2$ ($170x^+ \times 110z^+$), the FOV of the present implementation is considerably larger than that of the micro-pillar technique ($2.1 \times 2.1\,\mathrm{mm}^2$Liu et al. 2019) or DFRH ($1 \times 1\,\mathrm{mm}^2$, $20x^+ \times 20z^+$, Kumar et al. 2021) and µDH ($1.5 \times 1.5\,\mathrm{mm}^2$, $88x^+ \times 88z^+$, Sheng et al. 2008). Similarly, the depth-from-defocus approaches have a small FOV on the order of $1 \times 1\,\mathrm{mm}^2$ (Fuchs et al. 2023; Klinner and Willert 2024). The MEMS-based WSS “imagers" by Kimura et al. (1999) provided a FOV of $22 \times 7.5\,\mathrm{mm}^2$, however, on a relatively coarse grid of sensors consisting of 3 rows spaced at $\Delta x = 10\,\mathrm{mm}$ with 25 sensors each spaced at $\Delta z = 300\,\mu\mathrm{m}$. In this regard, the present work offers both a high spatio-temporal resolution on a FOV covering in excess of one mean wall streak spacing.

7 Conclusion and outlook

The material presented herein demonstrates the viability of event-based imaging velocimetry for accurate measurement of TBL properties by means of Lagrangian particle tracking, providing near-wall velocity profiles and WSS distributions along with derived quantities. The reduced data stream of EBV permits continuous recording on the order of minutes (or longer) using off-the-shelf computer systems for data storage. Uncertainties arising from the limited (1-bit) signal depth of the image data are accounted for by making use of the available temporal resolution of the raw data which is on the order of 5–10 kHz. Track reconstruction can be greatly improved using Wiener or Kalman filtering such as implemented by Borer et al. (2017).

Even without processing, the raw event data are well suited for the visualization of the near-wall dynamics. While this is also possible with high-speed particle imaging approaches, the inherent binary nature of the raw imagery captured by event cameras immediately provides high-contrast visualizations without additional effort (see, e.g., event data animations provided in the supplementary material, Appendix 2). In the present application, rapid spanwise modulations imparted by the passage of flow structures in the outer layers of the TBL are clearly visualized and suggest further spatio-temporal analysis of the dynamics to retrieve, for instance, the structure convection velocity.

The time-resolved data presented herein were acquired using hardware that is considerably cheaper in comparison with conventional high-speed PIV components necessary to achieve similar results and but, at this point, are unable to stream images for extended periods. Beyond this, the higher sensitivity of the EBV detectors reduces the power requirements of the laser used to illuminate the tracer particles.

The present measurements were performed at a laser pulsing frequency of 5 kHz. Although not discussed here, a small portion of data was also acquired at 10 kHz and provided acceptable results in spite of a partial leakage (overflow) of some events into the following laser pulse period. Given the same magnification and the frequency limit of about 10 kHz for the utilized event camera hardware, the proposed technique should be applicable to TBL flows with friction velocities approaching $u_\tau = 1\,\mathrm{m/s}$.

Appendix 1: Tracer characteristics in the viscous layer

As pointed out by Shih and Lumley (1993) the Kolmogorov velocity scale u_η near the wall is of the same magnitude as the friction velocity u_τ such that the length scale η is given by

$$\frac{\nu}{u_\tau} \approx \frac{\nu}{u_\eta} = \frac{\nu}{(\eta\epsilon)^{1/4}} = \eta. \tag{14}$$

Under the same premise, the Kolmogorov time scale $t_\eta = (\nu/\epsilon)^{1/2}$ is related to the shear strain rate at the wall

$$\left.\frac{\partial u}{\partial y}\right|_{y=0} = \frac{{u_\tau}^2}{\nu} \approx \frac{{u_\eta}^2}{\nu} = \frac{(\nu\epsilon)^{1/2}}{\nu} = \frac{1}{t_\eta}. \tag{15}$$

With the Kolmogorov microscales directly corresponding to the viscous scales the following quantities are obtained for the $U_\infty = 5.2\,\mathrm{m/s}$ flow condition: $\eta \approx 70\,\mu\mathrm{m}$, $t_\eta \approx 300\,\mu\mathrm{s}$ and $u_\eta \approx 0.22\,\mathrm{m/s}$. These quantities are of relevance for characterization of tracer particle performance described next.

A quantity describing a particle's fidelity of moving with the flow, that is, along the streamline, is the Stokes number given by the ratio of the particle response time t_p and the characteristic time scale of the flow t_f:

$$\mathrm{Stk} = \frac{t_p}{t_f} \quad \text{with} \quad t_p = \frac{1}{18}\frac{\rho_p d_p^2}{\mu_f} \tag{16}$$

for spherical particles of diameter d_p and density ρ_p carried in a fluid with dynamic viscosity μ_f. Values significantly smaller than $\mathrm{Stk} = 1$ indicate a good flow tracking performance.

The water-glycol droplets used in the present 3d LPT measurements have a size range of $[1\,\mu\mathrm{m} < d_p < 2\,\mu\mathrm{m}]$ with corresponding relaxation times of $[3\,\mu\mathrm{s} < t_p < 12\,\mu\mathrm{s}]$. In the viscous sublayer $t_f = t_\eta$ such that the Stokes number becomes $\mathrm{Stk} \leq 0.04$ at $U_\infty = 5.2\,\mathrm{m/s}$. At $U_\infty = 7.5\,\mathrm{m/s}$ the characteristic time scale decreases to $t_\eta \approx 165\,\mu\mathrm{s}$ with $\mathrm{Stk} \leq 0.07$. At the highest velocity of $U_\infty = 10.0$ m/s and $t_\eta \approx 100\,\mu\mathrm{s}$ the Stokes number further increases to $\mathrm{Stk} \leq 0.12$ for particles with $d_p \leq 2\,\mu\mathrm{m}$. Overall this indicates an adequate tracking performance, especially at the lower tunnel operating speed.

Appendix 2: Supplementary material

Animated sequences of the acquired event data and recovered near-wall particle tracks are provided as supplementary material.

- File **Suppl1-Events-Vel5mps-ts5ms-0.1x.mp4** - visualization of events captured by central camera at $U_\infty = 5.2\,\mathrm{m/s}$ at 0.1× actual speed; time-slice of 5 ms per pseudo-image (25 pulses per image), event rate 7.0×10^6 Events/s, positive events only.
- File **Suppl2-Events-Vel5mps-ts5ms-0.01x.mp4** - visualization of events captured by central camera at $U_\infty = 5.2\,\mathrm{m/s}$ at 0.01× actual speed; time-slice of 5 ms per pseudo-image (25 pulses per image), event rate 7.0×10^6 Events/s, positive events only.
- File **Suppl3-WSS-magnitude-200ms.mp4** - visualization of near-wall particle tracks color coded with magnitude of the wall shear stress (WSS). Only 3 most recent time steps of tracks are color coded, then fade from gray to black ($U_\infty = 5.2\,\mathrm{m/s}$, speed about 0.02× actual speed).

Supplementary Information The online version contains supplementary material available at https://doi.org/10.1007/s00348-024-03946-2.

Acknowledgements We are very appreciative of the support by our colleagues of DLR Institute of Aerodynamics and Flow Technology during our measurement campaign in Göttingen, in particular Prof. Markus Raffel and his team for the use of the wind tunnel facility and Prof. Andreas Schröder for providing the high-speed cameras for the high-speed profile PIV reference measurements.

Author contributions CW conceptualized and realized the event-based 3d tracking measurement technique. CW and JK jointly set up and performed the wind tunnel measurements and subsequently worked out the data processing strategies, event data processing codes, and accompanying data analysis; CW wrote the original draft of the manuscript, which was reviewed by JK and department colleagues.

Funding Open Access funding enabled and organized by Projekt DEAL. This work was made possible through DLR-internal funding.

Data availability Sample event data can be obtained from the author upon request.

Declarations

Conflict of interest There is no conflict of interest to declare.

Ethics approval Not applicable.

References

Beck C (2004) Superstatistics in hydrodynamic turbulence. Phys D 193(1):195–207. https://doi.org/10.1016/j.physd.2004.01.020

Benedict LH, Gould RD (1996) Towards better uncertainty estimates for turbulence statistics. Exp Fluids 22(2):129–136. https://doi.org/10.1007/s003480050030

Borer D, Delbruck T, Rösgen T (2017) Three-dimensional particle tracking velocimetry using dynamic vision sensors. Exp Fluids. https://doi.org/10.1007/s00348-017-2452-5

Bross M, Fuchs T, Kähler CJ (2019) Interaction of coherent flow structures in adverse pressure gradient turbulent boundary layers. J Fluid Mech 873:287–321. https://doi.org/10.1017/jfm.2019.408

Brücker C (2015) Evidence of rare backflow and skin-friction critical points in near-wall turbulence using micropillar imaging. Phys Fluids 27(3):031,705. https://doi.org/10.1063/1.4916768

Brücker C, Bauer D, Chaves H (2007) Dynamic response of micro-pillar sensors measuring fluctuating wall-shear-stress. Exp Fluids 42:737–749. https://doi.org/10.1007/s00348-007-0282-6

de Silva CM, Gnanamanickam EP, Atkinson C et al (2014) High spatial range velocity measurements in a high Reynolds number turbulent boundary layer. Phys Fluids 26(2):025,117. https://doi.org/10.1063/1.4866458

Diaz-Daniel C, Laizet S, Vassilicos JC (2017) Wall shear stress fluctuations: mixed scaling and their effects on velocity fluctuations in a turbulent boundary layer. Phys Fluids 29(5):055,102. https://doi.org/10.1063/1.4984002

Drazen D, Lichtsteiner P, Haefliger P et al (2011) Toward real-time particle tracking using an event-based dynamic vision sensor. Exp Fluids 51(1):1465–1469. https://doi.org/10.1007/s00348-011-1207-y

Fuchs T, Bross M, Kähler CJ (2023) Wall-shear-stress measurements using volumetric μPTV. Exp Fluids 64(6):115. https://doi.org/10.1007/s00348-023-03656-1

Gallego G, Delbrück T, Orchard G et al (2022) Event-based vision: a survey. IEEE Trans Pattern Anal Mach Intell 44(1):154–180. https://doi.org/10.1109/TPAMI.2020.3008413

Gehrig D, Scaramuzza D (2024) Low-latency automotive vision with event cameras. Nature 629:1034–1040. https://doi.org/10.1038/s41586-024-07409-w

Gnanamanickam EP, Nottebrock B, Große S et al (2013) Measurement of turbulent wall shear-stress using micro-pillars. Meas Sci Technol 24(12):124,002. https://doi.org/10.1088/0957-0233/24/12/124002

Große S, Schröder W (2008) Dynamic wall-shear stress measurements in turbulent pipe flow using the micro-pillar sensor MPS3. Int J Heat Fluid Flow 29(3):830–840. https://doi.org/10.1016/j.ijheatfluidflow.2008.01.008

Jeon S, Choi H, Yoo JY et al (1999) Space-time characteristics of the wall shear-stress fluctuations in a low-Reynolds-number channel flow. Phys Fluids 11(10):3084–3094. https://doi.org/10.1063/1.870166

Kimura M, Tung S, Lew J et al (1999) Measurements of wall shear stress of a turbulent boundary layer using a micro-shear-stress imaging chip. Fluid Dyn Res 24(6):329–342. https://doi.org/10.1016/S0169-5983(99)00002-7

Klinner J, Willert C (2024) Measurements of the unsteady wall shear stress vector using multi-aperture defocusing microscopic particle tracking velocimetry. Exp Thermal Fluid Sci. https://doi.org/10.1016/j.expthermflusci.2024.111395

Kumar SS, Huang X, Yang X et al (2021) Three dimensional flow motions in the viscous sublayer. Theor Appl Mech Lett 11(2):100,239. https://doi.org/10.1016/j.taml.2021.100239

Lagraa B, Labraga L, Mazouz A (2004) Characterization of low-speed streaks in the near-wall region of a turbulent boundary layer. Eur J Mech B Fluids 23(4):587–599. https://doi.org/10.1016/j.euromechflu.2003.12.005

Liu Y, Klaas M, Schröder W (2019) Measurements of the wall-shear stress distribution in turbulent channel flow using the micro-pillar shear stress sensor MPS3. Exp Thermal Fluid Sci 106:171–182. https://doi.org/10.1016/j.expthermflusci.2019.04.022

Mordant N, Crawford A, Bodenschatz E (2004) Experimental Lagrangian acceleration probability density function measurement. Phys D 193(1–4):245–251. https://doi.org/10.1016/j.physd.2004.01.041

Ni Z, Pacoret C, Benosman R et al (2012) Asynchronous event-based high speed vision for microparticle tracking. J Microsc 245(3):236–244. https://doi.org/10.1111/j.1365-2818.2011.03565.x

Örlü R, Schlatter P (2011) On the fluctuating wall-shear stress in zero pressure-gradient turbulent boundary layer flows. Phys Fluids 23(2):021,704. https://doi.org/10.1063/1.3555191

Örlü R, Vinuesa R (2020) Instantaneous wall-shear-stress measurements: advances and application to near-wall extreme events. Meas Sci Technol 31(11):112,001. https://doi.org/10.1088/1361-6501/aba06f

Quadrio M, Luchini P (2003) Integral space-time scales in turbulent wall flows. Phys Fluids 15(8):2219–2227. https://doi.org/10.1063/1.1586273

Robotics and Perception Group (2023) Event-based vision resources. https://github.com/uzh-rpg/event-based_vision_resources

Rusch A, Rösgen T (2023) TrackAER: real-time event-based quantitative flow visualization. Exp Fluids 64:136. https://doi.org/10.1007/s00348-023-03673-0

Schanz D, Gesemann S, Schröder A (2016) Shake-The-Box: Lagrangian particle tracking at high particle image densities. Exp Fluids 57(5):1–27. https://doi.org/10.1007/s00348-016-2157-1

Schlatter P, Örlü R (2010) Assessment of direct numerical simulation data of turbulent boundary layers. J Fluid Mech 659:116–126. https://doi.org/10.1017/S0022112010003113

Schröder A, Schanz D, Gesemann S et al (2015) Near-wall turbulence characterization using 4D-PTV Shake-The-Box. In: 11th International Symposium on Particle Image Velocimetry (ISPIV 2021), Santa Barbara (USA). https://core.ac.uk/download/pdf/31016523.pdf

Schröder A, Schanz D, Gesemann S et al (2022) Measurements of the energy dissipation rate in homogeneous turbulence using dense 3D Lagrangian particle tracking and FlowFit. In: Proceedings of the 20th International Symposium on the Application of Laser and Imaging Techniques to Fluid Mechanics, Lisbon, pp 2300–2319. https://elib.dlr.de/189080/

Schröder A, Schanz D, Geisler R et al (2024) Near-wall flow features in ZPG-TBL at various Reynolds numbers using dense 3d Lagrangian particle tracking. In: 21st International Symposium on Application of Laser and Imaging Techniques to Fluid Mechanics, Lisbon, Portugal. https://doi.org/10.55037/lxlaser.21st.226

Sheng J, Malkiel E, Katz J (2008) Using digital holographic microscopy for simultaneous measurements of 3d near wall velocity and wall shear stress in a turbulent boundary layer. Exp Fluids 45:1023–1035. https://doi.org/10.1007/s00348-008-0524-2

Shih TH, Lumley JL (1993) Kolmogorov behavior of near-wall turbulence and its application in turbulence modeling. Int J Comput Fluid Dyn 1(1):43–56. https://doi.org/10.1080/10618569308904463

Sillero JA, Jiménez J, Moser RD (2013) One-point statistics for turbulent wall-bounded flows at Reynolds numbers up to $\delta^+ \approx 2000$. Phys Fluids 25(10):105,102. https://doi.org/10.1063/1.4823831

Smith CR, Metzler SP (1983) The characteristics of low-speed streaks in the near-wall region of a turbulent boundary layer. J Fluid Mech 129:27–54. https://doi.org/10.1017/S0022112083000634

Stelzenmuller N, Polanco JI, Vignal L et al (2017) Lagrangian acceleration statistics in a turbulent channel flow. Phys Rev Fluids 2(054):602. https://doi.org/10.1103/PhysRevFluids.2.054602

Voth GA, La Porta A, Crawford AM et al (2002) Measurement of particle accelerations in fully developed turbulence. J Fluid Mech 469:121–160. https://doi.org/10.1017/S0022112002001842

Wang J, Pan C, Wang J (2020) Characteristics of fluctuating wall-shear stress in a turbulent boundary layer at low-to-moderate Reynolds number. Phys Rev Fluids 5(7):074605. https://doi.org/10.1103/PhysRevFluids.5.074605

Wang Y, Idoughi R, Heidrich W (2020) Stereo event-based particle tracking velocimetry for 3d fluid flow reconstruction. In: Vedaldi

A, Bischof H, Brox T et al (eds) Computer Vision - ECCV 2020. Springer International Publishing, Cham, pp 36–53. https://doi.org/10.1007/978-3-030-58526-6_3

Willert C (2023) Event-based imaging velocimetry using pulsed illumination. Exp Fluids 64:98. https://doi.org/10.1007/s00348-023-03641-8

Willert C, Klinner J (2022) Event-based imaging velocimetry: an assessment of event-based cameras for the measurement of fluid flows. Exp Fluids 63:101. https://doi.org/10.1007/s00348-022-03441-6

Willert C, Cuvier C, Foucaut J et al (2018) Experimental evidence of near-wall reverse flow events in a zero pressure gradient turbulent boundary layer. Exp Thermal Fluid Sci 91(Supplement C):320–328. https://doi.org/10.1016/j.expthermflusci.2017.10.033

Yeo K, Kim BG, Lee C (2010) On the near-wall characteristics of acceleration in turbulence. J Fluid Mech 659:405–419. https://doi.org/10.1017/S0022112010002557

Zamansky R, Vinkovic I, Gorokhovski M (2011) Acceleration statistics of solid particles in turbulent channel flow. Phys Fluids 23(11):113,304. https://doi.org/10.1063/1.3662006